Galactic cosmic radiation in the interplanetary space through a modern secular minimum

Space Weather

RESEARCH ARTICLE
10.1029/2019SW002428

Galactic Cosmic Radiation in the Interplanetary Space Through a Modern Secular Minimum

F. Rahmanifard[1,2], W. C. de Wet[1,2], N. A. Schwadron[1,2], M. J. Owens[3], A. P. Jordan[1,2], J. K. Wilson[1,2], C. J. Joyce[4], H. E. Spence[1,2], C. W. Smith[1], and L. W. Townsend[2,5]

[1]Space Science Center, University of New Hampshire, Durham, NH, USA, [2]Solar System Exploration Research Virtual Institute, NASA Ames Research Center, Moffett Field, CA, USA, [3]Space and Atmospheric Electricity Group, Department of Meteorology, University of Reading, Reading, UK, [4]Department of Astrophysical Sciences, Princeton University, Princeton, NJ, USA, [5]Department of Nuclear Engineering, University of Tennessee, Knoxville, Knoxville, TN, USA

Key Points:
- The Sun is exhibiting a persistent decline in solar activity, similar to past secular minima
- The GCR radiation doses will probably exceed the already unprecedentedly high values
- The radiation environment will be a limiting factor for long-term mission planning

Correspondence to:
F. Rahmanifard,
F.Rahmanifard@unh.edu

Citation:
Rahmanifard, F., de Wet, W. C., Schwadron, N. A., Owens, M. J., Jordan, A. P., Wilson, J. K., et al. (2020). Galactic cosmic radiation in the interplanetary space through a modern secular minimum. *Space Weather*, *18*, e2019SW002428. https://doi.org/10.1029/2019SW002428

Received 13 DEC 2019
Accepted 19 JUL 2020
Accepted article online 23 JUL 2020

Abstract Recent solar conditions indicate a persistent decline in solar activity—possibly similar to the past solar grand minima. During such periods of low solar activity, the fluxes of galactic cosmic rays (GCRs) increase remarkably, presenting a hazard for long-term crewed space missions. We used data from the Cosmic Ray Telescope for the Effects of Radiation (CRaTER) on the Lunar Reconnaissance Orbiter (LRO) to examine the correlation between the heliospheric magnetic field, solar wind speed, and solar modulation potential of the GCRs through Cycle 24. We used this correlation to project observations from past secular solar minima, including the Dalton minimum (1790–1830) and the Gleissberg minimum (1890–1920), into the next cycle. For the case of conditions similar to the Dalton (or Gleissberg) minimum, the heliospheric magnetic field could drop to 3.61 (or 4.06) nT, leading to a dose rate increase of ~75% (or 34%). We showed that accounting for a floor in the modulation potential, invoked by the Badhwar-O'Neill 2014 model, moderates the projected radiation levels in Cycle 25. We used these results to determine the most conservative permissible mission duration (PMD, $290.4^{+37.7}_{-35.9}$ and $204.3^{+26.6}_{-25.2}$ days for 45-year-old male and female astronauts, respectively) based on a 3% risk of exposure-induced death (REID) at the upper 95% confidence interval in interplanetary space.

1. Introduction

Human space missions beyond Earth's magnetic shielding will face the challenge of the deep space radiation environment, which is composed of galactic cosmic rays (GCRs) and solar energetic particles (SEPs). Solar flares and shock waves, driven by coronal mass ejections (CMEs), can produce SEPs. As a result, large SEPs are associated with acute radiation syndromes including short-term effects ranging from fatigue to the possibility of an in-flight fatality (Cucinotta et al., 2015). We use an online system, Predictions of radiation from REleASE (Relativistic Electron Alert System for Exploration), EMMREM (Earth-Moon-Mars Radiation Exposure Module), and Data Incorporating the CRaTER, COSTEP (COmprehensive SupraThermal and Energetic Particle analyzer), and other SEP measurements (PREDICCS; http://prediccs.sr.unh.edu), that provides a reliable near-real-time probability of SEPs (Joyce et al., 2013; Quinn et al., 2017; Schwadron et al., 2012).

GCRs are energetic charged particles, likely accelerated in supernova explosions (Ackermann et al., 2013). They consist of protons, heavier ions, and a small fraction of electrons. Most of these ions are filtered at the interface between the heliosphere and the interstellar medium. The remaining ions enter the heliosphere at a constant rate (see section 5), although, since they interact with the heliospheric magnetic field (HMF) (Jokipii, 1991; Parker, 1965), solar cycles affect their flux in the inner heliosphere. GCRs are typically much more energetic and thus more penetrating than SEPs. While SEPs sporadically exhibit large fluences over short periods of time, GCR flux is much lower in comparison but always present. As a result, GCRs are associated with long-term (cancer) effects that pose a lasting threat for the crew, particularly in long-duration missions (e.g., Cucinotta et al., 2001; Schwadron et al., 2014).

In order to design exploration missions in the inner heliosphere, both short-term and long-term effects of the radiation have been investigated (e.g., Cucinotta, 2014; Cucinotta & Durante, 2006; Cucinotta et al., 2001, 2010, 2015; Durante & Cucinotta, 2008; NRC, 2008, 2012). Ground radiation limits for radiation

workers were the basis for National Council on Radiation Protection and Measurements (NCRP, 2000) recommendations for excessive 3% cancer fatality risk dose limits. These ground limits are calculated based on effective dose, which accounts for tissue weightings. The 1-Sv effective dose is defined as the weighted equivalent of 1 J of radiation energy absorbed by 1 kg of tissue. Based on a 3% risk of exposure-induced death (REID), NRC (2008) established the dose limits: 620-mSv limit for a 30-year-old male and 470-mSv limit for a 30-year-old female. The 3% REID accounts for the deaths shifted to earlier ages due to radiation exposure, which is more limiting than the excess risk of cancer fatality. These dose limits were implemented by Schwadron et al. (2014) to obtain allowable days for mission duration in the coming solar cycles.

However, these exposure limits are subject to uncertainties mainly due to extrapolating cancer risk data from high to low dose rates, transferring risk across different populations, uncertainties in epidemiology data, and most importantly, the lack of knowledge on risks from heavy ions and secondary radiation in space (Cucinotta et al., 2010). Therefore, National Aeronautics and Space Administration (NASA) permissible exposure limits (PELs) based on NCRP recommendations (NCRP, 2000) and 3% REID (NRC, 2008) must be implemented with an upper bound of 95% confidence level. The Human Integration Design Handbook (2014) applied the 95% confidence level and reported effective dose limits for a 1-year mission for male and female astronauts (see National Aeronautics and Space Administration, 2014, Table 6.8-5). The de Wet et al. (2020) evaluation of the NASA risk model provides REID accumulation rates and the resulting PMD as a function of Al shielding thickness and solar modulation potential.

To design successful and safe missions for the coming years, it is important to predict the solar activity and the resulting radiation environment. It is possible that the current cycle is the beginning of an era of persistent decline in solar activity that is a secular (grand) minimum (see section 4). Smith et al. (2014) projected the HMF and solar wind proton flux until 2025 using Schwadron and McComas (2008) and Schwadron, Connick, and Smith, (2010) theories, assuming that the coming decade would resemble the Dalton or the Gleissberg minimum. In the case of a deep grand minimum the HMF becomes very weak, the solar wind becomes less dense, and the size of the heliosphere shrinks significantly. Also, the lower number of CMEs leads to fewer irregularities to inhibit the GCR diffusion, which in turn leads to higher GCR flux and associated risks.

In this paper, we focus on long-term risk of the radiation caused by GCRs. For more information on the SEP radiation effects, refer to Schwadron et al. (2018) and Cohen and Mewaldt (2018, etc). We use the upper bound of the 95% confidence level for 3% REID limits to find the most conservative PMD in interplanetary space for probable cases of a Dalton (or Gleissberg)-like minimum. In section 2, we review the Cosmic Ray Telescope for the Effects of Radiation (CRaTER) data used in this paper. In section 3, we give an overview of the GCRs and the modulation they undergo as they reach the inner heliosphere. In section 4, we discuss solar activity predictions that lead us to consider scenarios for a modern secular minimum. These scenarios and what they imply for the modulation of the GCRs are discussed in section 5. In section 6 we describe the radiation risks based on these scenarios and the limits they impose on space explorations. Concluding remarks are provided in section 7.

2. CRaTER Data

The CRaTER (Spence et al., 2010), on board the Lunar Reconnaissance Orbiter (LRO) (Tooley et al., 2010), aims to investigate the lunar radiation environment. CRaTER consists of three pairs of silicon detectors, each pair including one thin (odd-numbered) and one thick (even-numbered) detector. Two pieces of tissue equivalent plastic (TEP) are located between these pairs of detectors (See Figure 1, Schwadron et al., 2018). All these components are stacked along an axis perpendicular to the lunar surface, with the first pair of detectors (D1 and D2) facing zenith and the third pair (D5 and D6), facing nadir.

Silicon detectors measure deposited (lost) energy of incident energetic particles above 7 keV. The deposited energy divided by the path length of the incident particles is the linear energy transfer (LET). CRaTER is designed to cover the full range of LET expected by the SEPs and GCRs: there is an overlap between the detectable LET ranges in each detector pair. We correct this overlap by taking the deposited energy in the thin detector as the contributor (see Schwadron et al., 2012, for further details). Further, we include conversion from silicon to water: Schwadron et al. (2012) showed that for the GCR energy range of interest, a factor of 1.33 can be applied to the silicon dose to determine the dose in water. This result was also determined from the sums over energy depositions in the two materials over an appropriate range of LET. The energy

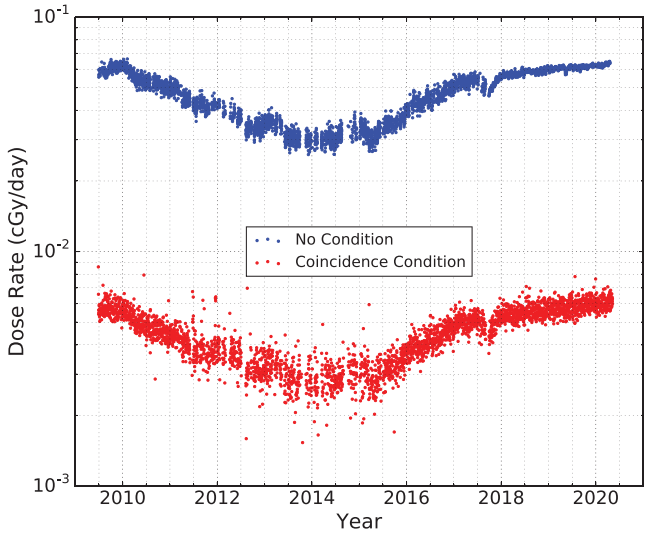

Figure 1. Comparing dose rates measured by D5 and D6 detector pair, projected to free space and converted to show dose rates deposited in water, with and without coincidence conditions. Blue circles represent CRaTER D5 and D6 detector pair dose rates with no coincidence conditions. Red circles represent D5 and D6 detector pair dose rates using the triple coincidence and the deposited energy in $D6 > D4 > D2$ conditions. These dose rates are also projected to free space to eliminate the effect of the triple coincidence condition limiting the field of view.

dependence of the ratio introduces an uncertainty in this conversion factor of about 5%, comparable to or smaller than other uncertainties in the measurement.

Incident particles from the sides of the instrument impose variations in the path length. In order to eliminate these side penetrators and thus reduce the path length distribution, coincidence conditions were introduced to the registered events. In this study, we use a triple coincidence condition so that each observed event must trigger Detectors D2, D4, and D6. An additional constraint is for the deposited energy in D6 to be greater than in D4 and the deposited energy in D4 to be greater than in D2. Since the rate of deposited energy increases as the particles slow down while traversing the instrument, this guarantees capturing incident particles from free space and excludes lunar albedo ions from the observed dose rates. Figure 1 shows the effect of these conditions on dose rates observed by CRaTER's third pair of detectors projected to free space.

As can be seen in Figure 1, requiring these conditions reduces the observed dose rates by an order of magnitude. This is expected since these conditions impose a species-dependent lower limit on the energy of the particles contributing to the dose rate. Moreover, the triple coincidence condition limits the field of view of the detector pair, which we have taken into account in the values presented in Figure 1 by projecting dose rates to free space. In order to use these observations to find the modulation potential that describes GCR radiation in free space, de Wet et al. (2020) passed the detailed geometry of the instrument into their model and produced effective modulation potential data applicable in free space. Furthermore, low-energy particles that are excluded by imposing the triple coincidence condition are the least significant in terms of exposure risk (see de Wet et al., 2020, for further details). Therefore, the dose rates from the third pair of detectors with the aforementioned criteria, shown in Figure 1, can be used for the purpose of this work. Figure 1 contains the most recent dose rates measured by D5 and D6 detector pair, projected to free space to be comparable to the dose rates presented in section 6.

3. Solar Modulation of GCRs

More than 90% of the GCRs are filtered by the slowed solar wind in the heliospheric interface with the local interstellar medium (LISM) (Florinski et al., 2003). This shielding decreases with a decrease in solar wind pressure and the size of the heliosphere (thus probably with long-term solar variations). While many questions remain about the nature of the LISM and its interaction with our heliosphere, observations from Interstellar Boundary Explorer (IBEX) (McComas et al., 2009) and Voyager 1 and 2 (Richardson et al., 2008; Stone et al., 2005) have greatly improved our understanding. Future observations from the Interstellar

Mapping and Acceleration Probe (IMAP) (McComas et al., 2018) will be helpful in obtaining a deeper understanding of the LISM environment, its interaction with the heliosphere, and its effects on the radiation environment of the inner heliosphere.

Radionuclides, such as ^{10}Be, are created by collisions between GCRs and atmospheric atoms and provide a long-term proxy for cosmic ray fluxes. There is a noticeable agreement between the HMF based on ^{10}Be sequestered in the polar ice cores (McCracken, 2007; McCracken & Beer, 2015), reconstructed HMF based on sunspot records (e.g., Owens et al., 2016, 2017; Rahmanifard et al., 2017), and geomagnetic data (e.g., Lockwood et al., 2013a, 2013b; Lockwood, Nevanlinna, Barnard, et al., 2014; Lockwood, Nevanlinna, Vokhmyanin, et al., 2014; Owens et al., 2016). This agreement suggests a steady anticorrelation between the Sun's activity and ^{10}Be flux, which demonstrates that the incoming flux entering the heliosphere and the filtration it has undergone in the boundary of the heliosphere have remained relatively unchanged in the last few centuries.

After being filtered by the shielding of the outer heliosphere, the residual GCRs are modulated by the HMF in the heliosphere. Therefore, they are subject to 11-year solar cycles, first noticed by Forbush (1954). The 22-year Hale cycles also affect the modulation of the GCRs. When the field lines in the Northern Hemisphere of the Sun are directed outward ($A > 0$, the second half of even cycles), the curvature of the field causes ions to drift down over the poles and outward near the equatorial current sheet. During these even $A > 0$ cycles, we observe a broad peak in the flux of positively charged GCRs such as GCR protons. Conversely, during the minimum of odd cycles ($A < 0$), ions travel into the heliosphere along the current sheet, where they encounter the irregularities in the current sheet and CMEs, convecting them out. As a result, access of positively charged GCRs to the inner heliosphere is more restricted during odd $A < 0$ cycles as compared to even $A > 0$ cycles. This leads to a sharp peak during odd $A < 0$ cycles in the GCR fluxes of positively charged GCRs (e.g., Webber & Lockwood, 1988).

The transport of GCRs in the interplanetary medium can be described by the modulation potential (Gleeson & Axford, 1968). The modulation potential (ϕ) is related to the rigidity ($P = pc/q$, where p is the particle momentum and q is the particle charge) of GCRs. The modulation potential approximately corresponds to the energy lost by GCR particles traveling from the LISM to the inner heliosphere. Assuming the diffusion coefficient is separable into radially and rigidity-dependent components, Badhwar and O'Neill (1994) provided a species-dependent model to determine the GCR flux over time using stationary solutions of the Fokker-Planck equation.

The High-charge (Z) and Energy (HZE) Transport code (HZETRN) uses a one-dimensional Boltzmann transport equation to solve analytically for the GCRs' interaction with materials (Cucinotta, 1993; Nealy et al., 2007; Wilson & Badavi, 1986; Wilson et al., 2003). As CRaTER was at early stages of its mission, an investigation of the radiation from GCRs during the prolonged minimum of Solar Cycle 23 showed that the weak modulation of GCRs could lead to the highest dose rates in a 25-year period between 1984 and 2009 (Schwadron, Boyd, et al., 2010). To further explore this era of low solar activity and its elevated radiation from GCRs, Schwadron, Townsend, et al. (2010) developed the EMMREM. EMMREM uses a three-layer version of HZETRN 2005 to obtain the GCR dose and other relevant quantities describing the radiation environment (Schwadron, Townsend, et al., 2010; Townsend et al., 2011).

An agreement between EMMREM results and CRaTER observations was reported by Schwadron et al. (2012). They compared dose rates predicted for the modulation potential from various sources including observations of neutrons using McMurdo data, the Advanced Composition Explorer (ACE) Cosmic Ray Isotope Spectrometer (CRIS), and in situ measurements of the HMF from the OMNI data set. OMNI compiles a set of data including near-Earth solar wind and magnetic field parameters from multiple sources. Schwadron et al. (2012) found an almost quadratic fit between the HMF and the modulation potential, compatible with the slab turbulence model of cosmic ray diffusion (le Roux et al., 1999). Fitting the modulation potential based on ACE data to the HMF reported by OMNI, Schwadron et al. (2012) inferred $\phi \propto |B|^{1.87}$. Using this power law, Schwadron et al. (2014) showed a correlation between the modulation potential and the mean solar magnetic field:

$$\phi = \phi_1 \left(\frac{V_{SW}}{V_1}\right)\left(\frac{|B|}{B_1}\right)^{\gamma} \quad (1)$$

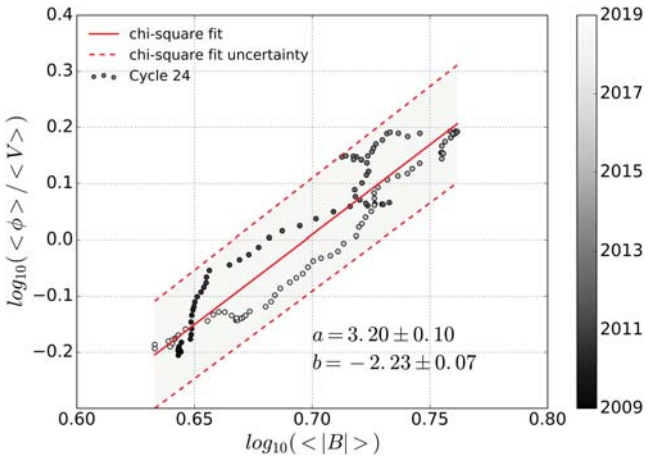

Figure 2. The correlation between the modulation potential, the HMF strength, and global solar wind speed is shown. The grayscale shows the sequence of time as the cycle proceeds, revealing a hysteresis behavior. We have used the modulation potential from CRaTER measurements (de Wet et al., 2020), HMF intensity from Rahmanifard et al. (2017), and global solar wind speed from Owens et al. (2017). A chi-square scheme was used to find a linear fit (red solid line), with a slope ($a = 3.20 \pm 0.10$) and an intercept ($b = -2.23 \pm 0.07$).

where $V_1 = 400$ km/s is a reference solar wind speed, $B_1 = 1$ nT is a reference magnetic field, $\phi_1 = 33.2$ MV is a reference modulation potential, and $\gamma = 1.87$.

To find these parameters, Schwadron et al. (2014) investigated the correlation between the modulation potential from ACE data (O'Neill, 2006) and CRaTER measurements (Joyce et al., 2014) with HMF and V_{SW} from OMNI data. However, as can be seen in Figure A1 of Schwadron et al. (2014), a departure is noticed from the correlation in Equation 1 during the solar maximum. They suggested that this departure could be attributed to globally merged interaction regions (GMIRs). GMIRs are large magnetic structures, which occur due to the pileup of interplanetary coronal mass ejections (ICMEs), corotating interaction regions (CIRs), and stream interaction regions (SIRs) in the outer heliosphere. They occur more frequently during phases of high solar activity and play a role in modulating GCRs (McDonald & Burlaga, 1997). However, more recent studies have investigated the role of CIRs in short-term modulation of GCRs near solar minima (Ghanbari et al., 2019).

In this study, we apply the same methodology using updated CRaTER measurements (2009–2019) to find a new correlation between the modulation potential from CRaTER and the HMF intensity (Figure 2). This modulation potential is obtained using dose rates measured by CRaTER applying a triple coincidence condition to remove side-penetrating particles (see section 2) based on a response function between dose rates observed by CRaTER and modulation potential (see de Wet et al., 2020, for further details). This response function is based on the BON14 model, while Schwadron et al. (2014) used BON2006 (O'Neill, 2006) to assign modulation potential values to dose rates measured by CRaTER. The absolute values of modulation potential in both versions of the BON model, however different they are, depend on arbitrarily chosen constants and thus are not significant. In this study, as in Schwadron et al. (2014) we investigate a linear correlation between ϕ/V and B in logarithmic space, based on Equation 1. Therefore, the obtained correlation and any further projections of the radiation environment based on this correlation is reliant on the accuracy of inferred solar parameters employed in this analysis. The HMF predictions were obtained from a sunspot-based model at 1 AU (Rahmanifard et al., 2017), in monthly resolution, and monthly global solar wind speed values were adopted from Owens et al. (2017). We used a least squares minimization method to find the slope $a = 3.20 \pm 0.10$ and intercept $b = -2.23 \pm 0.07$ of a linear fit to available data points. Since the absolute values of modulation potential in the BON14 model are different from the previous version, the parameters we found in this figure, mainly the slope, are significantly different from Schwadron et al. (2014). As can be seen in Figure 2, the departure from the correlation in the solar maximum, described in Schwadron et al. (2014), is also evident here, associated with the Years 2013 and 2014, when ϕ increases without a significant increase in B.

Additionally, in Figure 2, we have used gray circles with shades varying from the darkest in the beginning of solar cycle in 2009 to the lightest for our most recent available data points in 2018 to show the sequence of time. This grayscale reveals a trend in variations of the modulation potential with HMF, suggesting a hysteresis. Such hysteresis might be associated with Hale cycles, as we are currently in the second half of an even cycle ($A > 0$). At this time the structure of the magnetic field leads ions to drift in from poles of the Sun, where they avoid being scattered by irregularities near the current sheet, and therefore, their flux is enhanced over a broader period than in peaked odd $A < 0$ cycles. As a result, while B is increasing, ϕ does not increase as much, remains constant, or even decreases. Moreover, this hysteresis is also influenced by the remains of the HMF large-scale structures at the edge of the heliosphere, from a past solar maximum, still modulating the GCRs even after the Sun has started its declining phase.

4. Predictions of Solar Activity

Solar activity affects our space environment drastically, and therefore, its prediction is essential to space weather forecasting. It is well established that sunspot cycles are in phase with changes in the solar magnetic activity. Therefore, sunspot number has been widely used as a proxy for the level of solar activity. First attempts to predict solar activity using modeling techniques date back to Solar Cycle 21 (see Brown, 1986; McIntosh et al., 1979). Pesnell (2016) compared and categorized models predicting Solar Cycle 24 concluding that more reliable forecasts of solar activity require more advanced models based on data directly related to the solar magnetic field. Contrasting predictions of Solar Cycle 24 ranging from unprecedentedly low to unprecedentedly high amplitudes show that we are far from a consensus (for a thorough list of these models see Pesnell, 2014, 2016, and the references therein).

Upton and Hathaway (2018) predicted a Cycle 25 slightly weaker than Cycle 24 (5% weaker). Wang (2017) and Jiang and Cao (2018) also predicted Cycle 25 to be comparable to Cycle 24. There are a number of studies predicting Cycle 25 to be slightly stronger (e.g., Cameron et al., 2016; Helal & Galal, 2013; Yoshida, 2014). This might be the case since historically odd cycles are shown to display higher amplitudes than their adjacent even cycles. On the other hand, there are studies suggesting that next solar cycles will have much smaller amplitudes and lead us into deeper phases of a secular solar minimum (Shepherd et al., 2014).

The Solar Cycle 25 Prediction Panel (https://www.weather.gov/news/190504-sun-activity-in-solar-cycle) has predicted that the next cycle will be similar to the current cycle, start in late 2019 or 2020, peak in 2023–2026, and range in amplitude from 95 to 130 averaged daily sunspot numbers. The predicted situation is most similar to the beginning of the Gleissberg period in terms of the transition from an even cycle to an odd one with close amplitudes. However, there are still doubts about the length and amplitude of the next solar cycle. As we are resuming human deep space explorations, there is a need to consider scenarios close to deeper secular minima such as the Dalton minimum.

An expectation of the current low solar activity resembling the Dalton or Gleissberg minimum was previously reported (Smith et al., 2014). We updated their Figure 2 to show how realistic this expectation has been so far. In Figure 3, we show monthly averaged sunspot numbers from the Dalton and Gleissberg era (top panels) and compare them with the current cycle's observed sunspot numbers (bottom panels). In the bottom left, Cycle 5 (blue) is overlaid on Cycle 24 (black) persisting into Cycle 6 to show a possible Dalton-like condition. The bottom right panel demonstrates the same idea with Cycles 12 and 13 for a possible Gleissberg-like secular minimum. As can be seen in this figure Cycle 24 (smoothed maximum Sunspot Number 116.4) is stronger than Cycle 5 (smoothed maximum Sunspot Number 82.0) but slightly weaker than Cycle 12 (smoothed maximum Sunspot Number 124.4), likely suggesting that the next solar cycle will show a level of activity between what was observed for the Dalton and Gleissberg eras. Considering scenarios similar to these two secular minima for the next solar cycle provides an insight of possible radiation hazards as we are resuming long-term crewed space missions in deep space.

5. Extreme Scenarios for a Modern Minimum

Using a Dalton-like Cycle 25 (Figure 3) as an estimate for the deepest expected solar phase we might be experiencing in the coming decade, we can estimate an extreme scenario for the radiation environment. A Gleissberg-like Cycle 25 obtains a less alarming and probably more realistic condition. To investigate how these conditions affect the deep space radiation environment, we first apply the correlation acquired in section 3 to find the modulation potential using B (the HMF intensity) and V_{SW} (global solar wind). The

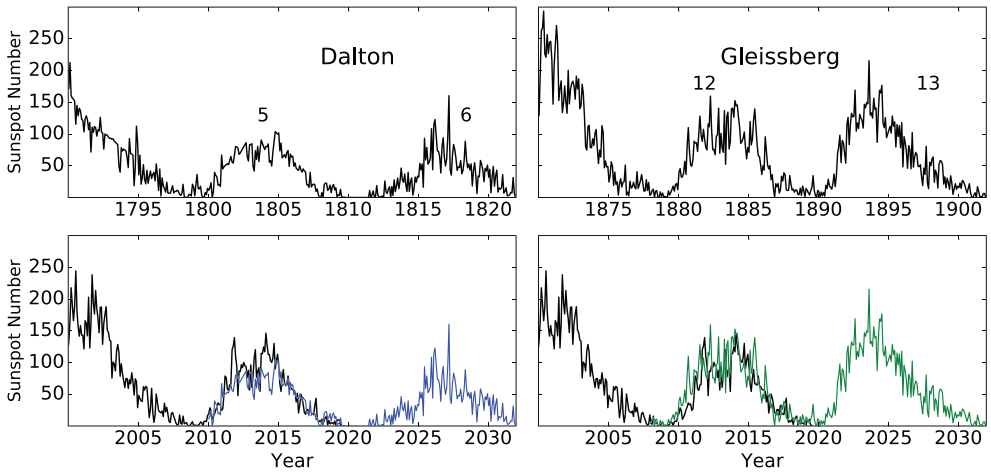

Figure 3. The recent decline in solar activity is compared to previous secular minima. The top left panel shows Cycles 5 and 6 (Dalton period), and in the bottom left these two cycles are laid over the current cycle. The top right panel shows Cycles 12 and 13 (Gleissberg period). In the bottom right, these two cycles are laid over Cycle 24.

HMF intensity was obtained from Rahmanifard et al. (2017) for sunspot numbers adopted from Cycle 6 (for a Dalton-like minimum) and Cycle 13 (for a Gleissberg-like minimum); V_{SW} was adopted from the Owens et al. (2017) reconstruction of the global solar wind speed for those cycles. The HMF intensity obtained by Rahmanifard et al. (2017) shows a good agreement with both OMNI and geomagnetic data through the least active phases of solar activity for which data are available: the Gleissberg secular minimum and the prolonged minimum of Cycle 23.

The slope and intercept of the correlation between the modulation potential, HMF, and solar wind speed might vary from cycle to cycle. However, in this study we applied the slope and intercept of Cycle 24 for the next solar cycle, assuming that the same condition holds for the next cycle. We postpone further investigation of previous cycles to a future publication. Assuming a Dalton-like or a Gleissberg-like minimum (Figure 4a) leads the modulation potential to decrease to values as low as $223.0 \pm 43.14MV$ (see Figure 5c). However, it is evident from the hysteretic shape of Cycle 24 shown in Figure 2 that not all phases of the cycle share the same slope. As can be seen in this figure, the slope decreases significantly as the cycle proceeds to a minimum. In particular, the very last data points in Figure 2 show a further decrease in the slope, likely suggesting that a prolonged solar minimum similar to the one observed for Cycle 23 might lead to even smaller slopes. This might suggest that, in the least active phases of a solar cycle, ϕ does not vary significantly with the decreasing HMF intensity, thus imposing a floor in the modulation potential.

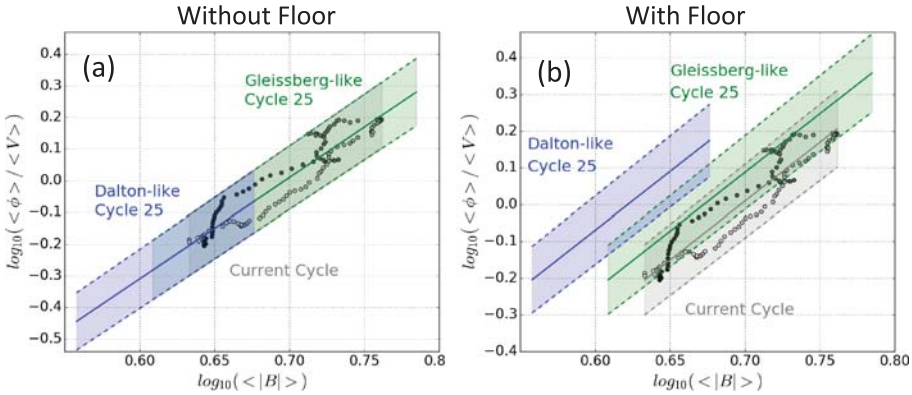

Figure 4. (a) The correlation acquired from Cycle 24 is applied to two possible scenarios for Cycle 25. The HMF strength for a Dalton-like and a Gleissberg-like Cycle 25 is calculated to find the modulation potential for these scenarios using the same slope and intercept from Figure 2. We used blue (green) lines and shaded uncertainty regions to show Dalton (Gleissberg) cases. (b) The same slope from Figure 2 and panel (a) is applied to the speculated Dalton (Gleissberg)-like Solar Cycle 25, applying the floor from BON14 ($\phi = 420.0$ MV).

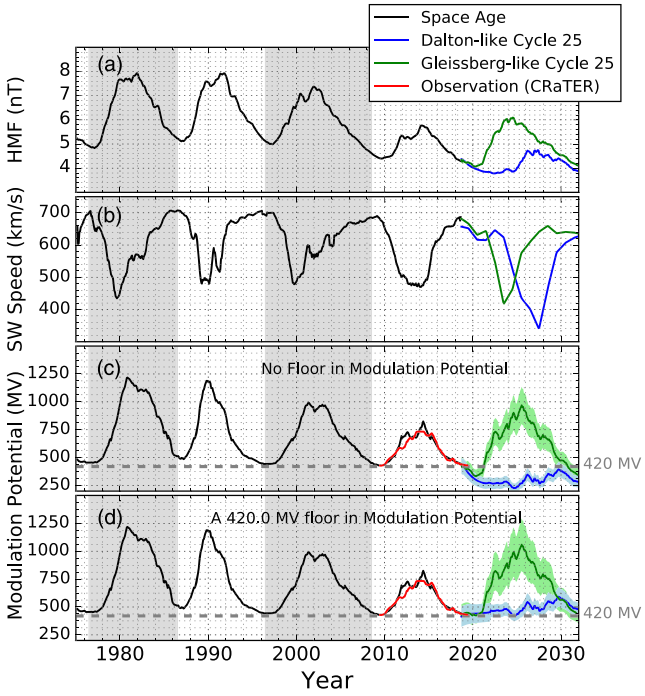

Figure 5. Panel (a) shows the HMF intensity through the space age (black) and extending to a speculated Cycle 25 (blue and green for Dalton-like and Gleissberg-like cases respectively). Panel (b) shows the global solar wind speed from Owens et al. (2017) using the same color code. Panels (c) and (d) show the modulation potential from BON14 through space age (black) and the modulation potential from CRaTER measurements in Cycle 24 (red). The modulation potential for a Dalton-like and a Gleissberg-like Cycle 25 based on the correlation from this work (Figure 4a) is shown in panel (c). Panel (d) shows the modulation potential for these two cases applying the floor in modulation potential from BON14 (using correlations in Figure 4b).

This floor can be associated with extensive filtration of the GCRs (with constant flux in the interstellar medium) by the accumulation of the large magnetic structures at the edge of the heliosphere. BON14 model assumes this filtration remains constant over time and as a result, the flux of the GCRs that enter the heliosphere remains constant as well. These remaining GCRs undergo solar modulation and their flux at 1 AU varies with the level of solar activity. However, it never exceeds the constant flux at the edge of the heliosphere, which dictates a floor in the modulation potential value. This approach ignores the possible effect of the long-term solar variations on the large magnetic structures at the edge of the heliosphere.

The absolute value of the modulation parameter in the BON14 model is based on arbitrarily chosen constants and thus is not significant. The values of ϕ in this model demonstrate the degree of modulation of the GCRs based on their choice of parameters. Additionally, the floor in the modulation parameter is imposed by their set of local interstellar (LIS) parameters describing the flux of GCR ions at 100 AU, where their modulation is negligible. The value obtained for the floor, 420 MV, is based on the observed relationship between sunspot number and GCR flux in the modern era (O'Neill et al., 2015). Currently, in the solar minimum of Cycle 24 we are very close to reaching this value.

The set of initial parameters in the BON14 model is obtained using satellite and balloon missions covering Cycles 20 to 24, which mostly falls into the modern solar maximum. However, the trend of weakening peak sunspot number associated with the solar maxima observed over the last 60 years indicates we could be moving into another grand minimum scenario. Since the floor in modulation potential present in the BON14 model has yet to be tested in a grand minimum scenario, it is possible that a persistent steep increase in the level of dose rates observed by CRaTER may lead to values smaller than the 420 MV floor embedded in BON14.

According to the correlation between HMF, solar wind speed, and solar modulation potential described in section 3, the value obtained for modulation potential based on CRaTER observations is expected to fall below the predicted floor if the current solar cycle persists into another prolonged deep minimum leading

us to grand minimum-like condition. If this is the case, the LIS modulation parameters within the BON14 model should be revised to account for the newly observed floor in modulation potential. Alternatively, as we are experiencing the second half of an even solar cycle, the flux of GCRs might end up in a flat peak, adhering to the floor predicted by LIS parameters used in the current version of the BON model.

A historic record of the BON predicted modulation potential shows that even through the weakest phases of solar activity, not only does the modulation value not fall below the floor but also this value increases and decreases with solar activity (de Wet et al., 2020). Therefore, to implement the floor predicted by the BON14 model, the modulation potential obtained based on Figure 4a was raised so that the minimum value of ϕ reached 420 MV. Increasing all ϕ values would have resulted in a discontinuity in the modulation potential values between observed values to this day and the projected values in Figure 5d. In order to avoid that, we assumed that the modulation potential does not vary significantly during the first year of the expected Cycle 25, resulting in a smooth transition between the two cycles in spite of different correlation patterns.

In Figure 5, we show the HMF intensity, global solar wind speed, and modulation potential since 1975, covering Solar Cycles 21–24 (black line) and extending to possible low solar activity scenarios for Cycle 25 (green and blue for Gleissberg-like and Dalton-like cases, respectively). In Figure 5a we show the HMF intensity adopted from Rahmanifard et al. (2017) who used sunspot reconstructed data as a proxy for the frequency of CMEs, as the source of closed magnetic flux (Owens & Crooker, 2006), to reconstruct a time series for the HMF based on the Schwadron, Connick, and Smith, (2010) theory (also see Solanki et al., 2000). In Figure 5b we show reconstructed global solar wind based on the Magnetohydrodynamics Algorithm outside a Sphere (MAS) model, which compares global magnetohydrodynamic (MHD) solutions to observed photospheric magnetograms (Owens et al., 2017).

Figures 5c and 5d present the modulation potential through the space age from BON14 model (black line), observed by CRaTER (red line), and for expected scenarios of a Gleissberg or Dalton-like Cycle 25 (green and blue lines, respectively, with shaded uncertainty regions). The projected modulation potential for Cycle 25 shown in Figure 5c is obtained by applying the correlation from Figure 4a. As can be seen, the modulation potential falls below the 420.0 MV floor embedded in BON14 model during the minimum phases of a Gleissberg-like Cycle 25 and throughout the whole cycle for a Dalton-like cycle. Implementing a 420.0 MV floor in the modulation potential raises these values, leading to more effective modulation of the GCRs in the next solar cycle as shown in Figure 5d. However, the Dalton-like case shown in Figure 5d still exhibits remarkably low modulation in the solar maximum and throughout the cycle.

We expect the pileup of the large magnetic structures to vary with long-term solar variations. As a result, we expect the filtration of GCRs at the edge of the heliosphere to be more efficient during secular maxima, similar to what was observed during space age and less efficient during secular (grand) minima. This might cause the flux of GCRs at the edge of the heliosphere to vary with long-term solar variations so that a single floor may not reflect the effect of long-term solar variations in the modulation of the GCRs. However, the current version of the BON model enforces a floor at 420 MV, which is reached at every solar minimum when the solar activity decreases to its minimum value. This floor is created to describe characteristics of the LIS spectrum through Solar Cycles 21 to 24. If Solar Cycle 25 is deeper than Cycle 24, a lower value for the floor in the modulation potential might be needed. However, entirely ignoring this floor may overlook the effect of shielding at the edge of the heliosphere. Therefore, in this paper, we investigated two cases: one using the correlation found for Cycle 24, without considering a change of slope during the minimum of Cycle 24, and one implementing the 420 MV floor predicted by BON14. We expect Solar Cycle 25 to lie somewhere between these two limiting cases.

6. Conservative Radiation Risks Based on Extreme Scenarios

A modulation potential-based response function was generated for the CRaTER instrument using the MCNP6 radiation transport code (de Wet et al., 2020). de Wet et al. (2020) passed the geometry of the instrument to a Monte Carlo transport code for various boundary condition fluxes associated with specific values of modulation potential and assembled the results into a response function. They used this response func-

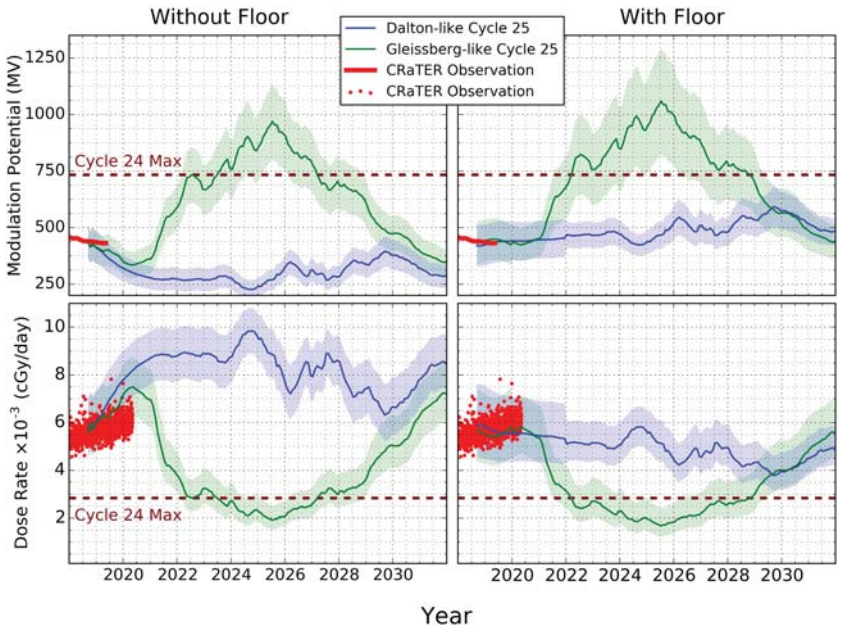

Figure 6. The top panels show the modulation potential for possible cases of a Dalton-like Cycle 25 and a Gleissberg-like Cycle 25 once using the correlation obtained from Figure 4a (without a floor, top left), and once using the correlation obtained in Figure 4b (with the floor, top right). The red solid line shows the most recent updates from CRaTER observations, which agrees with our projections of the modulation potential, especially for the case with a floor. The bottom panels present dose rates expected to be observed by CRaTER D5-D6 pair of detectors, projected to free space and converted to show dose rates deposited in water, with a triple coincidence condition for these cases. Red circles show the most recent updates from the CRaTER D5 and D6 pair of detectors observations. While the increase in the level of radiation is not as prominent as the case without a floor, its persistent increase is probably a sign that a further prolonged solar minimum similar to the Dalton era might lead to modulation values lower than the predicted floor. Dashed maroon lines show the observed values at the maximum of Cycle 24, adopted from de Wet et al. (2020).

tion to produce a modulation potential data set based on CRaTER observations. As mentioned in section 2, dose rates observed in the third pair of CRaTER detectors with a triple coincidence condition have been employed to create this modulation potential record since 2009. The resulting modulation potential record is shown in Figures 5c and 5d, in red.

Employing the CRaTER response function, we can use our projected modulation potential for an expected declining Solar Cycle 25 to project the worst-case radiation environment in deep space. We used this method to project D5 and D6 dose rates with a triple coincidence condition for the coming years (Figure 6). Additionally, we investigated the risks of a worsening radiation environment caused by a declining solar activity for future human space explorations. The risk model used in de Wet et al. (2020) includes the HZETRN code for male and female phantoms (known as MAX and FAX) in a spherical spacecraft exposed to a radiation environment associated with specific values of the modulation potential. They produced tables of effective dose rates and REID accumulation rates for male and female anatomies behind aluminum shielding ranging from 0.1 to 40 g/cm^2 for a modulation potential varying from 420 to 1,400 MV. We employed their results to find the 3% REID at 95% confidence level for 45-year-old astronauts, behind 20-g/cm^2 aluminum shielding, and the resulting PMD for expected scenarios for Cycle 25.

Figure 6 shows the modulation potential for a speculated modern minimum similar to the Dalton minimum (blue) or the Gleissberg minimum (green). In the top left panel, the modulation potential is presented based on a correlation shown in Figure 4a, assuming the same slope and intercept for Cycle 25 as was observed for Cycle 24. This assumption, when combined with a drastic decrease in the level of solar activity similar to what happened during the Dalton period, leads to a radical decrease in the modulation potential. As shown in the bottom left panel, such a decrease in the modulation of the GCRs leads to a further increase of the radiation hazard from the already unprecedentedly high radiation risks, particularly because a Dalton-like Cycle 25 will further extend the prolonged solar minimum of Cycle 24 for several years. A shallow delayed

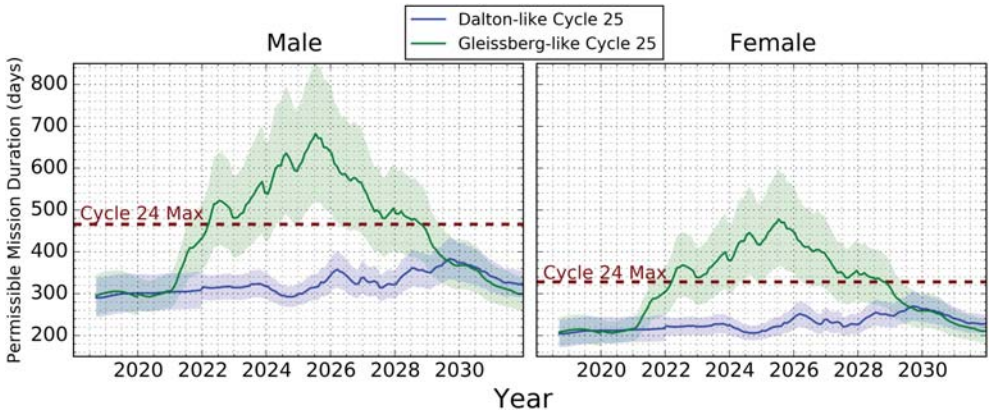

Figure 7. Projected PMD for possible cases of a Dalton-like Cycle 25 (blue) and a Gleissberg-like Cycle 25 (green) assuming a floor of 420.0 MV embedded in the BON14 holds in the deepest phases of solar activity (left, 45-year-old male astronaut; right, 45-year-old female astronaut). Dashed maroon line shows PMD value for male (female) astronauts at the maximum of Cycle 24, adopted from de Wet et al. (2020).

solar maximum similar to the one from Cycle 6 will not be able to effectively moderate such a radiation environment. A Gleissberg-like condition will not lead to a situation as dramatic. Particularly, a solar maximum similar to the observed maximum of Cycle 13 will recover the radiation environment by lowering dose rates to values smaller than the dose rates observed during the solar maximum of Cycle 24.

The right panels in Figure 6 are allocated to possible scenarios for Cycle 25 using a correlation illustrated in Figure 4b. We raised the modulation potential obtained based on Figure 4a so that the minimum value of the modulation potential reached a floor of 420 MV. The resulting modulation potential and dose rates are shown in the top right and bottom right panels of Figure 6, respectively. It is important to note that in this case, a further prolonged solar minimum associated with a Dalton-like Cycle 25 will not increase the dose rates any further. This means that in the absence of effective solar modulation and due to constant filtration at the edge of the heliosphere (assumed by the BON model) the flux of GCRs entering at the edge of the heliosphere remains constant, and hence, dose rates observed at 1 AU will not change significantly. Therefore, the projected dose rates for this case are significantly reduced compared to the previous case. Dose rates presented in Figure 6 are obtained from the response function in de Wet et al. (2020), but they are modified to include the conversion to LET in water and are projected to free space to be consistent with Figure 1. The red solid line (in the top panels) and red circles (in the bottom panel) present recent updates from CRaTER observations. While the increase in the level of radiation is not as prominent as in the case without a floor, its persistent increase might indicate that a further prolonged solar minimum similar to the Dalton era might result in modulation values lower than the BON predicted floor.

PMD values, based on a 3% REID at 95% confidence level, for these conditions, are presented in Figure 7 for 45-year-old astronauts (left for male and right for female) behind 20-g/cm^2 Al shielding. We show these values only for a case with a floor in the modulation potential since the risk model used in this study covers the modulation potential ranging from 420 to 1,400 MV. As a result, for both the Dalton-like and the Gleissberg-like scenarios the minimum PMD values are the same ($290.4^{+37.7}_{-35.9}$ days for male and $204.3^{+26.6}_{-25.2}$ days for female astronauts). PMD values remain low throughout a Dalton-like cycle, with slightly higher values for the maximum ($383.2^{+50.5}_{-48.2}$ days for male and $270.1^{+35.2}_{-34.3}$ days for female astronauts). For a Gleissberg-like scenario the maximum PMD values are significantly higher ($682.1^{+174.0}_{-159.1}$ days for male and $477.4^{+120.1}_{-109.0}$ days for female astronauts). Minimum and maximum values for the modulation potential and PMD time series presented in Figures 6 and 7 are summarized in Table 1).

Based on previously observed trends, odd cycles likely exhibit higher levels of activity than their adjacent even cycles (Yoshida, 2014). Therefore, Cycle 25 is expected to be slightly stronger than Cycle 24, resembling the solar cycle transition from Cycle 12 to Cycle 13 (during the Gleissberg period). However, Cycle 24 had a smaller amplitude than Cycle 12. This reinforces speculations that Cycle 25 will likely lead us to a deeper phase of a modern secular minimum—perhaps something between the Gleissberg and the Dalton minimum. Furthermore, the amount of shielding provided by the heliospheric interface likely decreases during extremely deep phases of grand (secular) minima. The BON14 model only relies on data from Cycles 20–24

Table 1
Minimum and Maximum Values Obtained for the Modulation Potential and Permissible Missions Duration (PMD) Based on a Dalton-Like and a Gleissberg-Like Cycle 25

		Modulation potential (MV)		PMD, male (days)		PMD, female (days)	
	Cycle 25 resembling	min.	max.	min.	max.	min.	max.
Without floor	Dalton	223.0 ± 43.14	433.0 ± 72.96				
	Gleissberg	330.1 ± 58.09	969.2 ± 166.1		$619.6^{+117.4}_{-110.0}$		$434.8^{+80.3}_{-75.8}$
With floor	Dalton	420.0 ± 71.45	591.9 ± 87.65	$290.4^{+37.7}_{-35.9}$	$383.2^{+50.5}_{-48.2}$	$204.3^{+26.6}_{-25.2}$	$270.1^{+35.2}_{-34.3}$
	Gleissberg	420.0 ± 71.45	1059.0 ± 235.0	$290.4^{+37.7}_{-35.9}$	$682.1^{+174.0}_{-159.1}$	$204.3^{+26.6}_{-25.2}$	$477.4^{+120.1}_{-109.0}$

Note. For the case without a floor, we have applied the correlation obtained for Cycle 24 to expected Cycle 25 scenarios. For the case with the floor, we have applied the same correlation and raised all modulation values so that the minimum values reach the 420-MV floor in BON14 model.

to obtain LIS parameters, during which we have mostly experienced a secular maximum; these values likely fail in accurately describing a deep minimum phase. Therefore, we expect the next solar cycle, if deeper than Cycle 24, to lie somewhere between these extreme cases.

7. Conclusion

Deep space radiation in the next decade or two may be more dangerous to interplanetary crews than previously realized. The minimum HMF has been in decline through the last few solar cycles and the protracted solar minimum of Cycles 23 and 24 along with the brief, weak solar maximum in Cycle 24 are consistent with an ongoing secular trend. Thus, the GCR fluxes in the inner solar system may increase more rapidly than previous estimates during the next solar cycle(s), which would be accompanied by a worsening radiation environment.

We have projected past secular minima conditions to find the modulation potential for Solar Cycle 25. We updated the correlation between the HMF, solar wind speed, and modulation potential from Schwadron et al. (2014) based on CRaTER data. We also obtained the HMF based on Rahmanifard et al. (2017), by assuming that the trend of decreasing solar activity will persist into the coming Cycle 25, using sunspot numbers from Gleissberg and Dalton periods. We applied the HMF found in this way and global solar wind speed expected for Gleissberg-like and Dalton-like Cycle 25 to find the modulation potential for these scenarios.

We found dose rates and PMDs from the modulation potential for Gleissberg-like and Dalton-like Cycle 25. We used the de Wet et al. (2020) evaluation of the NASA risk model to find dose rates and the resulting PMD from the modulation potential in the previous step. The PMD time series were calculated for 45-year-old astronauts, behind a 20-g/cm^2 nominal spacecraft shielding, based on a 3% REID at 95% confidence level, incorporating the 420.0-MV floor. Similar values were obtained for solar minimum of both Dalton-like and Gleissberg-like cycles: $290.4^{+37.7}_{-35.9}$ days for male and $204.3^{+26.6}_{-25.2}$ days for female astronauts.

These values are obtained for interplanetary space and thus are more limiting than scenarios where more shielding is provided by, for example, the lunar mass. Typically, transiting to the Moon and back to Earth takes a shorter time than the minimum PMD values found here. However, Mars missions demand more careful planning to avoid astronauts being exposed to GCRs radiation beyond the permissible durations presented here. Such planning must consider reducing the travel time by using higher-energy orbits and employing on-orbit staging, and more importantly, by considering transiting during phases of solar maximum.

For long-term space exploration during weak cycles, solar maximum is probably safer due to more effective modulation of the GCRs, despite the more frequent SEP events. The occurrence of the September 2017 event showed that, even during phases of low solar activity, discrete SEP events remain a significant hazard. Real-time monitoring of solar events would be essential to protect astronauts against such events with advance warning. In the future, we plan to investigate the radiation environment applicable to the deep space gateway and Artemis program by extending these results to the lunar radiation environment.

Data Availability Statement

CRaTER data are available online (at http://crater-web.sr.unh.edu).

Acknowledgments
We thank all those who made CRaTER possible. CRaTER is primarily funded by the LRO program (Contract NNG11PA03C). This work was also funded by DREAM2 (NASA Grant NNX14AG13A). The authors would like to thank Tony Slaba from NASA Langley Research Center for his guidance on the Badhwar O'Neill 2014 GCR and the NASA risk model.

References

Ackermann, M., Ajello, M., Allafort, A., Paglione, J., Petrovic, C., Taillefer, L., et al. (2013). Detection of the characteristic pion-decay signature in supernova remnants. *Science*, *193*(February), 807–811.

Badhwar, G. D., & O'Neill, P. M. (1994). Long-term modulation of galactic cosmic radiation and its model for space exploration. *International Journal of Radiation Applications and Instrumentation. Part*, *14*(10), 749–757. https://doi.org/10.1016/1359-0189(92)90024-P

Brown, G. (1986). Working Group "A" Report: Long-term solar activity predictions. In Simon, P. A., Heckman, G., & Shea, M. A. (Eds.), *Solar-rerrestrial predictions: Proceedings of a workshop at Meudon, France* pp. 1–7). Boulder, Colo.: Natl. Oceanic and Atmos. Admin.

Cameron, R. H., Jiang, J., & Schuessler, M. (2016). Solar cycle 25: Another moderate cycle?. *Astrophysical Journal Letters*, *823*(22), 5. https://doi.org/10.3847/2041-8205/823/2/L22

Cohen, C. M. S., & Mewaldt, R. A. (2018). The ground-level enhancement event of September 2017 and other large solar energetic particle events of Cycle 24. *Space Weather*, *16*, 1616–1623. https://doi.org/10.1029/2018SW002006

Cucinotta, F. A. (1993). Calculations of cosmic-ray helium transport in shielding materials: NASA Langley Research Center; Hampton, VA, United States.

Cucinotta, F. A. (2014). Space radiation risks for astronauts on multiple International Space Station missions. *PLoS ONE*, *9*(4), 96,099. https://doi.org/10.1371/journal

Cucinotta, F. A., Alp, M., Rowedder, B., & Kim, M. H. Y. (2015). Safe days in space with acceptable uncertainty from space radiation exposure. *Life Sciences in Space Research*, *5*, 31–38. https://doi.org/10.1016/j.lssr.2015.04.002

Cucinotta, F. A., & Durante, M. (2006). Essay. Cancer risk from exposure to galactic cosmic rays: Implications for space exploration by human beings. *Lancet Oncology*, *7*, 431–435. https://oncology.thelancet.comvol, .

Cucinotta, F. A., Hu, S., Schwadron, N. A., Kozarev, K., Townsend, L. W., & Kim, M. H. Y. (2010). Space radiation risk limits and Earth-Moon-Mars environmental models. *Space Weather*, *8*, S00E09. https://doi.org/10.1029/2010SW000572

Cucinotta, F. A., Schimmerling, W., Wilson, J. W., Peterson, L. E., Badhwar, G. D., Saganti, P. B., & Dicello, J. F. (2001). Space radiation cancer risks and uncertainties for Mars missions. *Radiation Research*, *156*, 682–8. https://www.ncbi.nlm.nih.gov/pubmed/11604093

de Wet, W. C., Slaba, T. C., Rahmanifard, F., Wislon, J. K., Jordan, A. P., Townsend, L. W., et al. (2020). CRaTER observed permissible mission duration for human operations in deep space. *Life Sciences in Space Research*, *26*, 149–162. https://doi.org/10.1016/j.lssr.2020.04.004

Durante, M., & Cucinotta, F. A. (2008). Heavy ion carcinogenesis and human space exploration. *Nature Reviews Cancer*, *8*, 465–472.

Florinski, V., Zank, G. P., & Pogorelov, N. V. (2003). Galactic cosmic ray transport in the global heliosphere. *Journal of Geophysical Research*, *108*(6), 1228. https://doi.org/10.1029/2002JA009695

Forbush, S. E. (1954). World-wide cosmic-ray variations, 1973–1952. *Journal of Geophysical Research*, *59*(4), 525–542.

Ghanbari, K., Florinski, V., Guo, X., Hu, Q., & Leske, R. (2019). Galactic cosmic rays modulation in the vicinity of corotating interaction regions: Observations during the last two solar minima. *The Astrophysical Journal*, *882*(1), 54. https://doi.org/10.3847/1538-4357/ab31a5

Gleeson, L. J., & Axford, W. I. (1968). Solar modulation of galactic cosmic rays. *The Astrophysical Journal*, *154*, 1011. https://doi.org/10.1086/149822

Helal, H. R., & Galal, A. A. (2013). An early prediction of the maximum amplitude of the solar cycle 25. *Journal of Advanced Research*, *4*(3), 275–278. https://doi.org/10.1016/j.jare.2012.10.002

Jiang, J., & Cao, J. (2018). Predicting solar surface large-scale magnetic field of cycle 24. *Journal of Atmospheric and Solar-Terrestrial Physics*, *176*, 34–41. https://doi.org/10.1016/j.jastp.2017.06.019

Jokipii, J. R. (1991). Variations of the cosmic-ray flux with time. In Sonett, P. C., Giampapa, M. S., & Matthews, M. S. (Eds.), *The Sun in time* (pp. 205–220). Tucson: University of Arizona Press.

Joyce, C. J., Schwadron, N. A., Wilson, J. K., Spence, H. E., Kasper, J. C., Golightly, M., et al. (2013). Validation of PREDICCS using LRO/CRaTER observations during three major solar events in 2012. *Space Weather*, *11*, 350–360. https://doi.org/10.1002/swe.20059

Joyce, C. J., Schwadron, N. A., Wilson, J. K., Spence, H. E., Kasper, J. C., Golightly, M., et al. (2014). Radiation modeling in the Earth and Mars atmospheres using LRO/CRaTER with the EMMREM Module. *Space Weather*, *12*, 112–119. https://doi.org/10.1002/2013SW000997

le Roux, J. A., Zank, G. P., & Ptuskin, V. S. (1999). An evaluation of perpendicular diffusion models regarding cosmic ray modulation on the basis of a hydromagnetic description for solar wind turbulence. *Journal of Geophysical Research*, *104*(A11), 24,845–24,862. https://doi.org/10.1029/1999ja900318

Lockwood, M., Barnard, L., Nevanlinna, H., Owens, M. J., Harrison, R. G., Rouillard, A. P., & Davis, C. J. (2013a). Reconstruction of geomagnetic activity and near-Earth interplanetary conditions over the past 167 yr—Part 1: A new geomagnetic data composite. *Annales Geophysicae*, *31*(11), 1957–1977. https://doi.org/10.5194/angeo-31-1957-2013

Lockwood, M., Barnard, L., Nevanlinna, H., Owens, M. J., Harrison, R. G., Rouillard, A. P., & Davis, C. J. (2013b). Reconstruction of geomagnetic activity and near-Earth interplanetary conditions over the past 167 yr—Part 2: A new reconstruction of the interplanetary magnetic field. *Annales Geophysicae*, *31*(4), 1979–1992. https://doi.org/10.5194/angeo-31-1979-2013

Lockwood, M., Nevanlinna, H., Barnard, L., Owens, M. J., Harrison, R. G., Rouillard, A. P., & Scott, C. J. (2014). Reconstruction of geomagnetic activity and near-Earth interplanetary conditions over the past 167 yr—Part 4: Near-Earth solar wind speed, IMF, and open solar flux. *Annales Geophysicae*, *32*(4), 383–399. https://doi.org/10.5194/angeo-32-383-2014

Lockwood, M., Nevanlinna, H., Vokhmyanin, M., Ponyavin, D., Sokolov, S., Barnard, L., et al. (2014). Reconstruction of geomagnetic activity and near-Earth interplanetary conditions over the past 167 yr—Part 3: Improved representation of solar cycle 11. *Annales Geophysicae*, *32*(4), 367–381. https://doi.org/10.5194/angeo-32-367-2014

McComas, D. J., Allegrini, F., Bochsler, P., Bzowski, M., Christian, E. R., Crew, G. B., et al. (2009). Global observations of the interstellar interaction from the Interstellar Boundary Explorer (IBEX). *Science*, *326*(5955), 959–962. https://doi.org/10.1126/science.1180906

McComas, D. J., Christian, E. R., Schwadron, N. A., Fox, N., Westlake, J., Allegrini, F., et al. (2018). Interstellar Mapping and Acceleration Probe (IMAP): A new NASA mission. *Space Science Reviews*, *214*(8), 116. https://doi.org/10.1007/s11214-018-0550-1

McCracken, K. G. (2007). Heliomagnetic field near Earth, 1428–2005. *Journal of Geophysical Research*, *112*, A09106. https://doi.org/10.1029/2006JA012119

McCracken, K. G., & Beer, J. (2015). The annual cosmic-radiation intensities 1391–2014; The annual heliospheric magnetic field strengths 1391–1983, and identification of solar cosmic-ray events in the cosmogenic record 1800–1983. *Solar Physics*, *290*(10), 3051–3069. https://doi.org/10.1007/s11207-015-0777-x

McDonald, F. B., & Burlaga, L. F. (1997). Global merged interaction regions. In Jokipii, J. R., Sonett, C. P., & Giampapa, M. S. (Eds.), *Cosmic winds and the heliosphere* (pp. 581–616). Tucson: Univ. of Ariz. Press.

McIntosh, P. S., Brown, G. M., Buhmann, R., Clark, T., Fougere, P. F., & Hunter, H. (1979). Long-term solar activity predictions. In Donnelly, R. (Ed.), *NASA. Marshall Space Flight Center Solar-Terrest. Predictions Proc.* (pp. 246–257). Boulder, Colo.: NOAA.
National Council on Radiation Protection and Measurements (NCRP) (2000). Radiation protection guidance for activities in low-Earth orbit (*NCRP Tech. Rep. 132*). Bethesda, Md.: Natl. Counc. on Radiat. Prot. and Meas.
NRC (2008). Managing space radiation risk in the new era of space exploration. Washington, D.C.: Natl. Acad. Press.
NRC (2012). Technical evaluation of the NASA model for cancer risk to astronauts due to space radiation. Washington, D. C.: Natl. Acad. Press.
National Aeronautics and Space Administration (2014). NASA handbook NASA/SP-2010-3407/REV1 National Aeronautics and Space Administration. Washington, DC: National Aeronautics and Space Administration.
Nealy, J. E., Cucinotta, F. A., Wilson, J. W., Badavi, F. F., Dachev, T. P., Tomov, B. T., et al. (2007). Pre-engineering spaceflight validation of environmental models and the 2005 HZETRN simulation code. *Advances in Space Research*, *40*(11), 1593–1610. https://doi.org/10.1016/j.asr.2006.12.029
O'Neill, P. M. (2006). Badhwar-O'Neill galactic cosmic ray model update based on Advanced Composition Explorer (ACE) energy spectra from 1997 to present. *Advances in Space Research*, *37*(9), 1727–1733. https://doi.org/10.1016/j.asr.2005.02.001
O'Neill, P. M., Golge, S., & Slaba, T. C. (2015). NASA-TP-2015-218569-Badhwar-O'Neill 2014 galactic cosmic ray flux model description (*March*). Houston: NASA Johnson Space Center.
Owens, M. J., Cliver, E., McCracken, K. G., Beer, J., Barnard, L., Lockwood, M., et al. (2016). Near-Earth heliospheric magnetic field intensity since 1750: 1. Sunspot and geomagnetic reconstructions. *Journal of Geophysical Research: Space Physics*, *121*, 6048–6063. https://doi.org/10.1002/2016JA022529
Owens, M. J., & Crooker, N. U. (2006). Coronal mass ejections and magnetic flux buildup in the heliosphere. *Journal of Geophysical Research*, *111*, A10104. https://doi.org/10.1029/2006JA011641
Owens, M. J., Lockwood, M., & Riley, P. (2017). Global solar wind variations over the last four centuries. *Nature Publishing Group*, *7*(January), 1–11. https://doi.org/10.1038/srep41548
Parker, E. N. (1965). The passage of energetic charged particles through interplanetary space. *Planetary and Space Science*, *13*(1), 9–49.
Pesnell, W. D. (2014). Predicting Solar Cycle 24 using a geomagnetic precursor pair. *Solar Physics*, *289*(6), 2317–2331. https://doi.org/10.1007/s11207-013-0470-x
Pesnell, W. D. (2016). Predictions of Solar Cycle 24: How are we doing? *Space Weather*, *14*, 10–21. https://doi.org/10.1002/2015SW001304
Quinn, P. R., Schwadron, N. A., Townsend, L. W., Wimmer-Schweingruber, R. F., Case, A. W., Spence, H. E., et al. (2017). Modeling the effectiveness of shielding in the Earth-Moon-Mars radiation environment using PREDICCS: Five solar events in 2012. *Journal of Space Weather and Space Climate*, *7*, A16. https://doi.org/10.1051/swsc/2017014
Rahmanifard, F., Schwadron, N. A., Smith, C. W., McCracken, K. G., Duderstadt, K. A., Lugaz, N., & Goelzer, M. L. (2017). Inferring the heliospheric magnetic field back through Maunder Minimum. *The Astrophysical Journal*, *837*(2), 165. https://doi.org/10.3847/1538-4357/aa6191
Richardson, J. D., Liu, Y., Wang, C., & McComas, D. J. (2008). Determining the LIC H density from the solar wind slowdown. *Astronomy & Astrophysics*, *491*, 1–5. https://doi.org/10.1051/0004-6361:20078565
Schwadron, N. A., Baker, T., Blake, B., Case, A. W., Cooper, J. F., Golightly, M., et al. (2012). Lunar radiation environment and space weathering from the Cosmic Ray Telescope for the Effects of Radiation (CRaTER). *Journal of Geophysical Research*, *117*, E00H13. https://doi.org/10.1029/2011JE003978
Schwadron, N. A., Blake, J. B., Case, A. W., Joyce, C. J., Kasper, J., Mazur, J., et al. (2014). Special section: Does the worsening galactic cosmic radiation environment observed by CRaTER preclude future manned deep space exploration ? *Space Weather*, *12*, 622–632. https://doi.org/10.1002/2014SW001084.Received
Schwadron, N. A., Boyd, A. J., Kozarev, K., Golightly, M., Spence, H., Townsend, L. W., & Owens, M. J. (2010). Galactic cosmic ray radiation hazard in the unusual extended solar minimum between Solar Cycles 23 and 24. *Space Weather*, *8*, S00E04. https://doi.org/10.1029/2010SW000567
Schwadron, N. A., Connick, D. E., & Smith, C. W. (2010). Magnetic flux balance in the heliosphere. *The Astrophysical Journal*, *722*(September), 132–136. https://doi.org/10.1088/2041-8205/722/2/L132
Schwadron, N. A., & McComas, D. J. (2008). The solar wind power from magnetic flux. *The Astrophysical Journal*, *686*(2003), L33–L36.
Schwadron, N. A., Rahmanifard, F., Wilson, J., & Jordan, A. P. (2018). Update on the Worsening Particle Radiation Environment Observed by CRaTER and implications for future human deep-space exploration. *Space Weather*, *16*, 289–303. https://doi.org/10.1002/2017SW001803
Schwadron, N. A., Townsend, L., Kozarev, K., Dayeh, M. A., Cucinotta, F., Desai, M., et al. (2010). Earth-Moon-Mars radiation environment module framework. *Space Weather*, *8*, S00E02. https://doi.org/10.1029/2009SW000523
Shepherd, S. J., Zharkov, S. I., & Zharkova, V. V. (2014). Prediction of solar activity from solar background magnetic field variations in Cycles 21–23. *Astrophysical Journal*, *795*(1), 46. https://doi.org/10.1088/0004-637X/795/1/46
Smith, C. W., McCracken, K. G., Schwadron, N. A., & Goelzer, M. L. (2014). The heliospheric magnetic flux, solar wind proton flux, and cosmic ray intensity during the coming solar minimum. *Space Weather*, *12*, 499–507. https://doi.org/10.1002/2014SW001067
Solanki, S. K., Schüssler, M., & Fligge, M. (2000). Evolution of the Sun's large-scale magnetic field since the Maunder minimum. *Nature*, *408*(6811), 445–447. https://doi.org/10.1038/35044027
Spence, H. E., Case, A. W., Golightly, M. J., Heine, T., Larsen, B. A., Blake, J. B., et al. (2010). CRaTER: The cosmic ray telescope for the effects of radiation experiment on the Lunar Reconnaissance Orbiter mission. *Space Science Reviews*, *150*(1-4), 243–284. https://doi.org/10.1007/s11214-009-9584-8
Stone, E. C., Cummings, A. C., McDonald, F. B., Heikkila, B. C., Lal, M., & Webber, W. R. (2005). Voyager 1 explores the termination shock region and the heliosheath beyond. *Science*, *309*(5743), 2017–2020. https://doi.org/10.1126/science.1117684
Tooley, C. R., Houghton, M. B., Saylor, R. S., Peddie, C., Everett, D. F., Baker, C. L., & Safdie, K. N. (2010). Lunar Reconnaissance Orbiter mission and spacecraft design. *Space Science Reviews*, *150*(1-4), 23–62. https://doi.org/10.1007/s11214-009-9624-4
Townsend, L. W., Pourarsalan, M., Cucinotta, F. A., Kim, M. Y., & Schwadron, N. A. (2011). Transmission of galactic cosmic rays through Mars atmosphere. *Space Weather*, *9*, S00E11. https://doi.org/10.1029/2009SW000564
Upton, L. A., & Hathaway, D. H. (2018). An updated Solar Cycle 25 prediction with AFT: The Modern Minimum. *Geophysical Research Letters*, *45*, 8091–8095. https://doi.org/10.1029/2018GL078387
Wang, Y. M. (2017). *Surface flux transport and the evolution of the Sun's polar fields*, vol. 210: Springer Netherlands. https://doi.org/10.1007/s11214-016-0257-0
Webber, W. R., & Lockwood, J. A. (1988). Characteristics of the 22-year modulation of cosmic rays as seen by neutron monitors. *Journal of Geophysical Research*, *93*(A8), 8735. https://doi.org/10.1029/ja093ia08p08735

Wilson, J. W., & Badavi, F. F. (1986). Methods of galactic heavy ion transport. *Radiation Research*, *108*(3), 231–237. https://doi.org/10.2307/3576911

Wilson, J. W., Nealy, J. E., de Angelis, G., Clowdsley, M. S., & Badavi, F. F. (2003). Deep space environment and shielding. In *AIP Conference Proceedings*, AIP Publishing, pp. 993–1010. https://doi.org/10.1063/1.1541395

Yoshida, A. (2014). Difference between even- and odd-numbered cycles in the predictability of solar activity and prediction of the amplitude of Cycle 25. *Annales Geophysicae*, *32*(8), 1035–1042. https://doi.org/10.5194/angeo-32-1035-2014